

Toward Seismic Metamaterials: The METAFORET Project

by Philippe Roux, Dino Bindi, Tobias Boxberger, Andrea Colombi, Fabrice Cotton, Isabelle Douste-Bacque, Stéphane Garambois, Philippe Gueguen, Gregor Hillers, Dan Hollis, Thomas Lecocq, and Ildut Pondaven

ABSTRACT

We report on a seismic metamaterial experiment in a pine-tree forest environment where the dense collection of trees behaves as subwavelength coupled resonators for surface seismic waves. For the METAFORET experiment, more than 1000 seismic sensors were deployed over a 120 m × 120 m area to study the properties of the ambient and induced seismic wavefield that propagates in the ground and in trees. The goal of the experiment was to establish a link between seismic-relevant scales and microscale and mesoscale studies that pioneered the development of metamaterial physics in optics and acoustics. The first results of the METAFORET experiment show the presence of frequency band gaps for Rayleigh waves associated with compressional and flexural resonances of the trees, which confirms the strong influence that a dense collection of trees can have on the propagation of seismic waves.

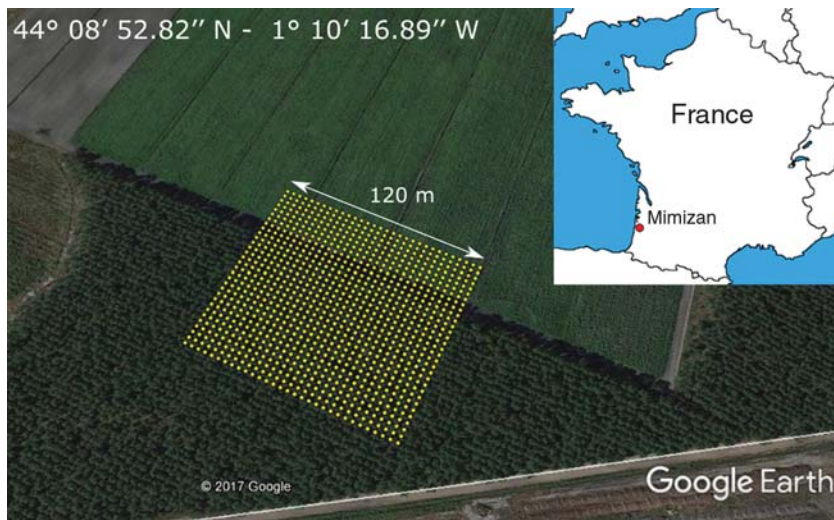
INTRODUCTION

Wave propagation phenomena that are not part of the response of natural materials arise in synthetic/manufactured composite materials due to the spatial ordering and/or resonance properties of the material constituents (Kittel and McEuen, 1976; Pendry *et al.*, 1999). Multiply scattered waves in a structurally ordered medium can lead to anomalous dispersion curves and frequency band gaps that emerge from constructive and/or destructive interference. In contrast, the mesoscale behavior of a composite material that consists of resonant elements with spatial disorder at the subwavelength scale is controlled by the dispersive nature of its coupled resonators (Liu *et al.*, 2000; Pendry, 2000; Engheta and Ziolkowski, 2006). Coupled subwavelength resonators define so-called locally resonant metamaterials. Their properties are governed by the interference between the incident and the scattered waves, which can lead to hybridized wavefields (Lemoult *et al.*, 2011). In this case, the spatial organization of the material is no longer relevant, and any frequency band gaps are independent of the ordering state (Kaina *et al.*, 2013). On the other hand, the possibility to control and manipulate waves at different scales

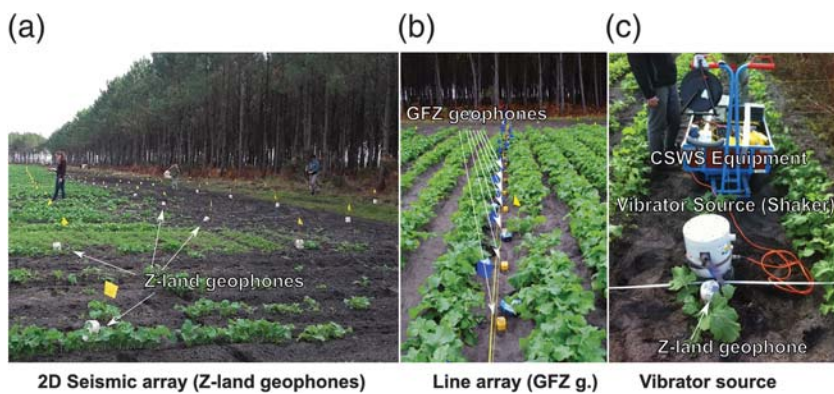
through specific spatial arrangements of resonators has allowed the realization of super lenses that can focus below the diffraction limit, and of different trial configurations toward invisibility cloaks (Leonhardt, 2006; Pendry *et al.*, 2006; Zhu *et al.*, 2011; Rupin *et al.*, 2015). The fundamental nature and robustness of these phenomena were demonstrated by the transfer of the earlier experiments from optical wave manipulation to recent acoustic experimentation (Milton *et al.*, 2006; Brun *et al.*, 2009). Other laboratory-scale investigations of elastic surface waves in thin plates supported by numerical experiments have also been performed to support the application of metamaterial physics to plate waves (Farhat *et al.*, 2009).

In the METAFORET experiment, it is the trees-in-the-ground configuration that constitutes the composite seismic metamaterial. Such phenomena are being studied at this scale for the first time, to investigate the scaling behavior of metamaterial physics. The ground–tree seismic metamaterial is expected to also induce frequency band gaps where seismic surface wave propagation is inhibited by the interactions between the induced wavefields and each of the trees, which act as resonators. The collective behavior of the trees would then be analogous to the results observed at the laboratory scale for optical, acoustic, and mechanical metamaterials. In particular, we expect complex and anomalous dispersion curves to generate subwavelength and suprawavelength modes that are similar to those observed in laboratory experiments with thin 60-cm-long vertical rods glued to a 2-m-wide, 6-mm-thick metallic plate (Rupin *et al.*, 2014). The successful upscaling depends on the characteristics of the Rayleigh-wave coupling with the trees (Colombi, Roux, *et al.*, 2016), and whether this captures the essential physics that controls the phenomena observed in the plate model, which is governed by simpler 2D propagation in a controlled laboratory environment.

The METAFORET project is paving the way to the development of seismic metamaterials with potential future applications in terms of seismic hazard and/or earthquake engineering in urban environments. If forests prove to be efficient natural structures for the reduction of anthropic ambient vibrations above 20 Hz, then tall buildings in urban areas



▲ **Figure 1.** Aerial view of the seismic deployment (yellow dots) at the interface between a canola field and a dense forest and localization of the experiment near Mimizan, France.



▲ **Figure 2.** Pictures of the METAFORET experiment seismic deployment: (a) the 2D geophone array made of 31×31 Z-land sensors positioned on a 4-m spacing x - y grid marked with yellow flags before they were buried in the ground on the first day of the deployment stage. (b) The 1D line array of Geophysical Instrument Pool Potsdam (GIPP) three-component geophones made of 100 sensors with 1-m spacing (blue flags) deployed perpendicular to the forest–field boundary. (c) The vibrator source (so called shaker) was positioned at 122 different locations during the METAFORET experiment to create controlled seismic sources. The shaker is a continuous surface-wave system from GDS Inc. that is composed of 70 kg vibrator powered by a power generator and controlled by a PC. The source signal was a 60-s-long frequency sweep from 10 to 100 Hz.

can potentially also behave as coupled resonators at much lower frequencies (Guéguen *et al.*, 2002; Guéguen and Bard, 2005; Guéguen and Colombi, 2016). The long-term objective of the METAFORET project is to determine whether buildings can form underground lenses for the bending or deflection of damaging seismic surface-wave motion below 5 Hz.

The unaliased spatial sampling of the complex forest wavefield across a wide range of frequencies includes the 40–50 Hz band gap target range that was suggested in a preliminary

numerical study (Colombi, Guenneau, *et al.*, 2016). This sampling requires a dense seismic network that consists of > 1000 seismic instruments in area of just $120 \text{ m} \times 120 \text{ m}$ (Figs. 1 and 2a,b). In the following, we describe the two-week deployment of the METAFORET experiment in October 2016 in the Landes forest (southwest France). We discuss all relevant aspects of the dense array continuous recording systems, the seismic vibrator source used to excite high-frequency transient wavefields (Fig. 2c; hereafter, the shaker), and the ground-penetrating radar (GPR) survey for high-resolution imaging of the top 2 m. We show the preliminary results of the ambient noise and active-source seismic wavefield analysis, in comparison with records of the tree-mounted velocimeters (Fig. 3), to illustrate the characteristic aspects of the frequency-dependent propagation regimes. We also introduce the numerical approach to investigate the details of the interaction between the trees and the seismic waves that propagate in the complex soil structure. Finally, we indicate where the publicly available data, metadata, processed data, and additional information on the METAFORET experiment can be retrieved.

THE EXPERIMENT

Seismic Network and Sensors

The site of this experiment is adjacent to the municipal airfield of the town of Mimizan, along the French Atlantic coast, about 100 km southwest of Bordeaux (Fig. 1). The experiment covers a square area of $120 \text{ m} \times 120 \text{ m}$ (Fig. 4a). The geophones cover 90 m of state-managed pine-tree forest and 30 m of an adjacent agricultural field where small canola plants were being grown at the time of the deployment (15–31 October 2016). The coordinate x is oriented parallel to the forest edge, and y is perpendicular to the forest edge (Fig. 4a). The trees grow along regular lines in the x direction, with a 4-m line interval in the y direction (Fig. 4b). The intraline tree distances δx are less regular, but are $\sim 2.5 \text{ m}$ on average. Each tree location within the area of interest was logged. To facilitate the seismic deployment and the GPR subsurface investigation, the interline brush was cleared by the state authorities using heavy equipment, and the experimental team continued this with the manual clearing of the remaining vegetation.

The seismic network consists of 995 Z-land vertical-component geophones (FairField Nodal Inc., see Data and Resources), 100 three-component geophones (Geophysical Instrument Pool Potsdam [GIPP]; see Data and Resources), and



Tree with 6 velocimeters attached

▲ **Figure 3.** Picture of one tree instrumented with 6 three-component Lennartz 1 s velocimeters positioned along the tree trunk at different heights and connected to the 24 bits CityShark digital acquisition system.

10 three-component velocimeters attached to a set of tree trunks at 2 m above the ground (Fig. 3).

The Z-land wireless technology includes a vertical geophone, a digitizer, a battery, a storage system, and a Global Positioning System (GPS) in a single box. This allowed the rapid deployment of the 995 geophones within three days (Fig. 2a). Each node was buried in the ground, up to the collar. The geophone has a lower corner frequency of 5 Hz. The sampling rate was set to 400 samples per second. The name of each node reflects its location within the grid system, which was made up of 31 lines and 31 columns, with 4-m interelement spacing in both x and y directions. In addition to the 31×31 geophones buried at each grid point (total, 961), two nodes were ground coupled on each side of the vibrator source, and the remaining 32 geophones were buried at the base of 32 neighboring trees along two lines inside the forest parallel to the x direction. The nodes recorded continuously for two weeks, after which they were collected and returned to the Geokinetics central acquisition facility in Houston, Texas, to download the raw data. The raw data were converted from a proprietary format to the MSEED format, using ObsPy func-

tions (see more information at see [Data and Resources](#); [Beyreuther et al., 2010](#)).

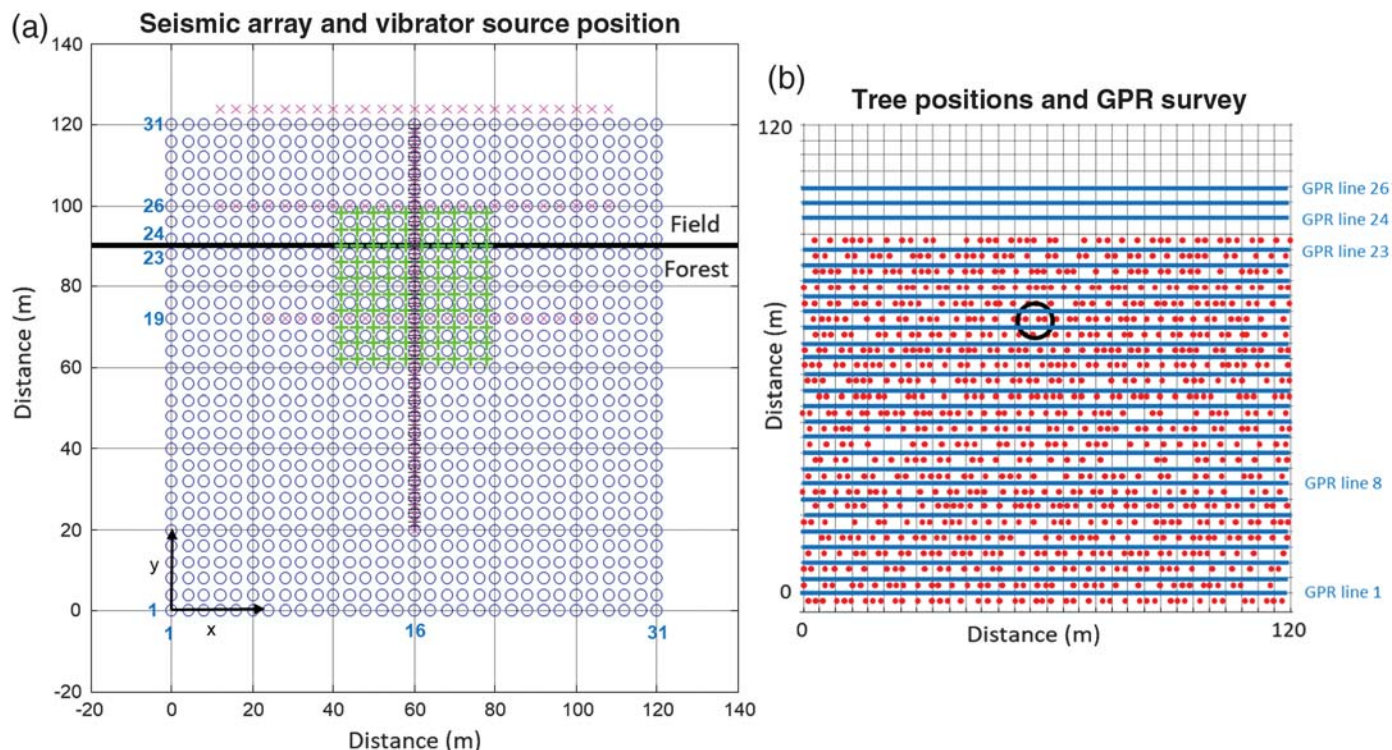
The experiment was strengthened by data from 100 seismic stations from the GIPP that were equipped with a DATA-CUBE3 recorder (see [Data and Resources](#)) connected to a three-component 4.5-Hz geophone (Fig. 2b). The DATA-CUBE3 was developed for short-term geophysical experiments with the optimization of the dimensions ($10 \times 10 \times 8.3 \text{ cm}^3$), weight (1 kg, including batteries), and power consumption (maximum runtime with two D-cell batteries, up to 14 days using cycled GPS settings). In the METAFORSET experiment, the GIPP instruments were deployed with built-in GPS, with the gain set to the maximum, the sampling rate set to 400 Hz, and performing continuous recording with the data stored on a 64-GB SDHC card. Technical information and software for translating the proprietary data format into MSEED were provided by the GIPP through its webpages.

The 100 GIPP instruments were used in two different spatial configurations, and continuously recorded both the ambient noise field and the controlled signals emitted by the shaker. The first configuration was deployed on 18 October 2016 (day 296), for four days, as a 10×10 square with equidistant 4-m spacing along both the x and y directions (Fig. 4a, green “+” marks). This smaller 10×10 array was interleaved in-between the 31×31 geophone array, which created a very dense 20×20 array with 2-m spacing at the border between the field and the forest. The second configuration was deployed on 23 October 2016 (day 299), for three days, as a 100-m line array with constant 1-m spacing (Fig. 4a, black crosses). It was located in the central $x = 60 \text{ m}$ and extended from $y = 20 \text{ m}$ to $y = 120 \text{ m}$, in which $y = 90 \text{ m}$ marks the field–forest boundary.

The Shaker as an Active Controlled Source

The shaker was a 70-kg continuous surface-wave system (GDS Inc.; see [Data and Resources](#)) that excites a 60-s-long, 10–100 Hz frequency-modulated sweep. The output gain of the continuous surface-wave system was set adaptively to prevent saturation of the recorded signals from two Z-land nodes located next to the vibrator source. At each source position (Fig. 4a, pink cross), the sweep emission was repeated five times, to allow for further coherent averaging. The sweep emission was recorded at each sensor of the seismic network, and further cross correlated with the emitted sweep for the pulse compression. This signal processing methodology (i.e., transmission of a frequency-modulated sweep that is cross correlated at each receiver with the emitted signal) mimics the transmission of a loud and broadband pulse in the bandwidth of interest.

A series of four line sources were defined during the course of the experiment. Three lines consisted of 21–25 separate sources (with 4 m separation between two successive sources) and were located parallel to the field–forest interface (Fig. 4a), both inside and outside the forest. Another line with 51 sources was acquired perpendicular to this interface (with 2 m separation between the two successive sources), with 17 sources in the field and 34 sources in the forest. This particular line source was collocated with the second GIPP deployment (the line



▲ **Figure 4.** Geometry of the METAFORET experiment: (a) spatial representation of the 2D seismic array composed of 31×31 vertical Z-land sensors (blue circles) and three-component GIPP instruments positioned as a 10×10 seismic array (green “+” marks) or a 100 sensors line array (black “+” marks) crossing the boundary between the field and the forest (horizontal bold black line). The shaker source was positioned at 122 different locations (pink “x” marks) involving three lines of sources along the x axis and a line along the y axis. Some column and row numbers (blue) have been added on the left and bottom sides of the 2D. (b) Spatial representation of the tree positions (red dots) projected on the 2D seismic grid (black line). The black circle surrounds trees that were instrumented by three-component velocimeters. Extra Z-land sensors were positioned at the bottom of each instrumented tree for deconvolution purpose. The horizontal blue lines correspond to the ground-penetrating radar (GPR) survey with 23 lines inside the forest and 3 lines in the open field. Note that the two panels (a) and (b) were drawn with the same distance scale.

array of 100 geophones), thus realizing the equivalent of an active seismic survey at the scale of the METAFORET experiment.

Velocimeters in Trees for Resonance Monitoring

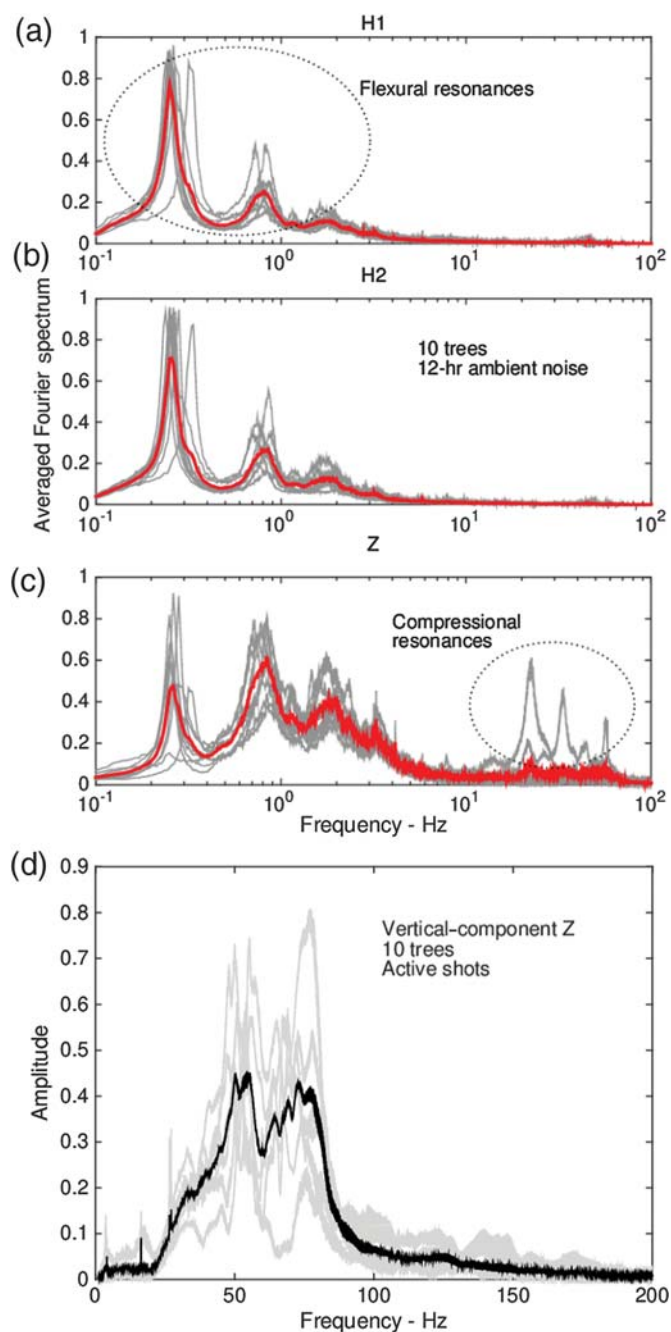
In combination with these seismic array deployments, two temporary experiments were performed to determine the interactions of the wavefield, with each tree considered as a resonator under ambient vibration and active-source excitation. Three-component velocimeters (Lennartz 3C 1 s) were connected to the Cityshark stations (Chatelain *et al.*, 2000) to record the tree vibrations. These sensors have a flat response between 1 and 70 Hz, and were mounted in several trees (Fig. 4b, black circles). They provided seismic records below the ~ 5 Hz cutoff frequency of the Z-land and GIPP sensors.

In a first configuration, operative modal analysis using ambient vibration recorded in one selected tree (at the center of the METAFORET configuration) was performed in the same way as experiments on civil engineering structures. Frequency domain decomposition (e.g., Brincker *et al.*, 2001; Michel *et al.*, 2010) was applied to a vertical array of six

velocimeters attached to one tree along the trunk (Fig. 3). The second configuration consisted of one velocimeter installed in each of six neighboring trees, at 2.5 m above the ground, and attached to each tree by a steel plate anchored rigidly to the trunk (Fig. 4b). Continuous 1-hr datasets were recorded over different periods of the experiments, including the quiet nighttime period and the active-source experiments. For example, Figure 5a–c shows the mean frequency spectrum during the 12 hrs of ambient noise records at night, whereas Figure 5d shows the vibrating frequency response of a set of trees during a shaker source experiment. In this particular case, the vertical impulse response of each tree was obtained by deconvolution of the vertical component recorded in the tree by the vertical-component ground motion recorded by the remaining Z-land sensors positioned at the bottom of each tree during the shaker experiments.

The Ground-Penetrating Radar Survey

The GPR data were acquired along the 120-m-long lines within the seismological network. The objective of the GPR survey was to assess the layered subsurface structure, to allow



▲ **Figure 5.** Normalized Fourier spectra of the ambient vibrations recorded in 10 instrumented trees during a night along (a) H1 (north), (b) H2 (east), and (c) vertical (Z) directions. Gray curves are the averaged Fourier spectra of a 12-hr-long recording window and the red curves are the average response of the trees. (d) Vertical impulse response of 10 instrumented trees (gray lines) computed by deconvolution between the tree velocimeter and the bottom Z-land sensor during the shaker source sequence performed perpendicular to the forest-field boundary (Fig. 4a). Bold black line corresponds to the average frequency response. For both ambient noise and active shots, the spectra were normalized by the global maximum of the three-component spectra (H1, H2, and Z). Note that (d) has a linear frequency axis in contrast to (a)–(c).

for further interpretation of the seismic signals recorded. A combination of 26 lines was recorded parallel to the forest-field interface, with 23 lines inside the forest and three lines in the canola field (Fig. 4b, blue horizontal lines). The goal was to image the main horizontal interfaces within the top 2 m. To ensure satisfactory resolution and sufficient penetration, the GPR data were acquired using 500 MHz shielded antennae (Mala Geosciences). The GPR acquisition was completed with common midpoint surveys, using 200 MHz unshielded antennae to estimate the vertical velocity distribution.

PRELIMINARY RESULTS

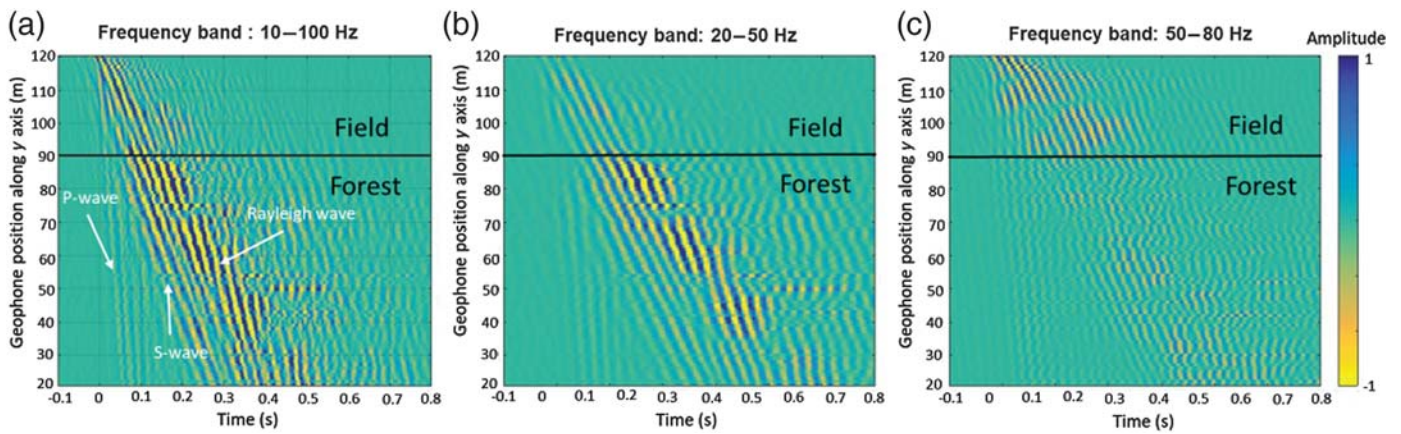
Velocimeter Data in the Trees

The modal analysis performed using Fourier analysis of ambient noise records shows clear resonances close to 0.3, 0.9, and 2 Hz, which correspond to the 3 first flexion modes of the trees. Figure 5a–c shows the normalized Fourier spectra for both horizontal components of the trees (H1, H2, corresponding to north and east directions), which were computed using ambient vibrations. All of the trees showed identical modes (except for one tree, with a fundamental frequency shifted to the highest frequency from the mean spectrum), allowing the homogeneity of the vertical resonators in the METAFORÉ experiment to be assumed at first sight. Along the vertical component, coupled modes at low frequencies with horizontal flexion are visible due to the amplitude of the vibration recorded in the tree that prevents the Z component from remaining motionless. At higher frequencies (e.g., > 10 Hz), the vertical motion clearly dominates the spectra (Fig. 5c) and appears to be very sensitive to the tree characteristics (i.e., diameter, height, boundary conditions at the bottom).

To confirm this behavior of the vertical component, vertical impulse responses of the trees were computed using the water-level deconvolution (Clayton and Wiggins, 1976; Nakata and Snieder, 2014), considering the Z-land sensor positioned at the bottom of each tree as the input signal. Ten responses of the trees are shown in Figure 5d. We show the vertical response of the trees during the sequence of shaker source experiments carried out perpendicular to the field-forest interface (Fig. 4a, pink crosses along the y axis). The mean frequency responses were computed considering the subset of closest shaker source experiments with high signal-to-noise ratio. After deconvolution, the vertical impulse response of each tree was obtained, with the separation of the soil-tree interactions from the tree response itself. In Figure 5d, the vertical response of the trees appears between 40 and 80 Hz, at a maximum at 50 Hz, which leads to a strong coupling with surface waves in this frequency band.

Seismic Wavefield

The seismic data consist of the active data, as the collection of the dynamic responses to each of the 122 controlled signals emitted from the shaker source, and the passive data, as the ambient noise recordings (analyzed during the nighttime) over 10 consecutive days of the METAFORÉ experiment.



▲ **Figure 6.** Spatiotemporal representation of the seismic field received on the vertical component of the 100-m-long line array of GIPP geophones (from position $[x = 60 \text{ m}, y = 120 \text{ m}]$ to position $[x = 60 \text{ m}, y = 20 \text{ m}]$) for a shaker source at position $(x = 60 \text{ m}, y = 120 \text{ m})$. The black line represents the forest–field boundary. The three panels correspond to different frequency filtering applied to the raw data: (a) raw data; (b) 20–50 Hz frequency band; and (c) 50–80 Hz frequency band. The seismic wavefield shows a clear transition at frequency $F_c = 50 \text{ Hz}$ that corresponds to the average compressional resonance frequency of the trees.

Figure 6 shows a distance-versus-time seismic section of the vertical component obtained from the source positioned at one end ($x = 60 \text{ m}, y = 120 \text{ m}$) of the 100-m-long GIPP line array that starts in the field 30 m before the field–forest interface, and ends 70 m further, far inside the forest ($x = 60 \text{ m}, y = 20 \text{ m}$). The 1 m spacing between the GIPP receivers provides a continuous pattern for waves that travel from outside to inside the forest. Three types of waves are visible in the seismic section (Fig. 6a), fast ($\sim 1000 \text{ m/s}$) and low-amplitude direct P waves, slower ($\sim 400 \text{ m/s}$) and moderate-amplitude direct S waves, and slow ($\sim 350 \text{ m/s}$) Rayleigh surface waves with variable amplitudes and time–space dispersion patterns. When filtering this wavefield pattern into two different bands below and above $F_c = 50 \text{ Hz}$, there were striking results for the surface waves, as expected from the velocimeter-in-tree analysis. Below F_c , there was an increase in the Rayleigh-wave amplitude as it penetrated into the forest (Fig. 6b). On the contrary, above F_c , the Rayleigh wave appeared to be damped at the interface between the field and the forest, even though some residual seismic energy can be observed again, at 30 m inside the forest (Fig. 6c). From these frequency-filtered seismic sections, the difference between the field and the forest was clearly visible for surface waves. The increase in surface-wave amplitude below F_c is typical of a metamaterial that has a forbidden frequency band that starts at F_c .

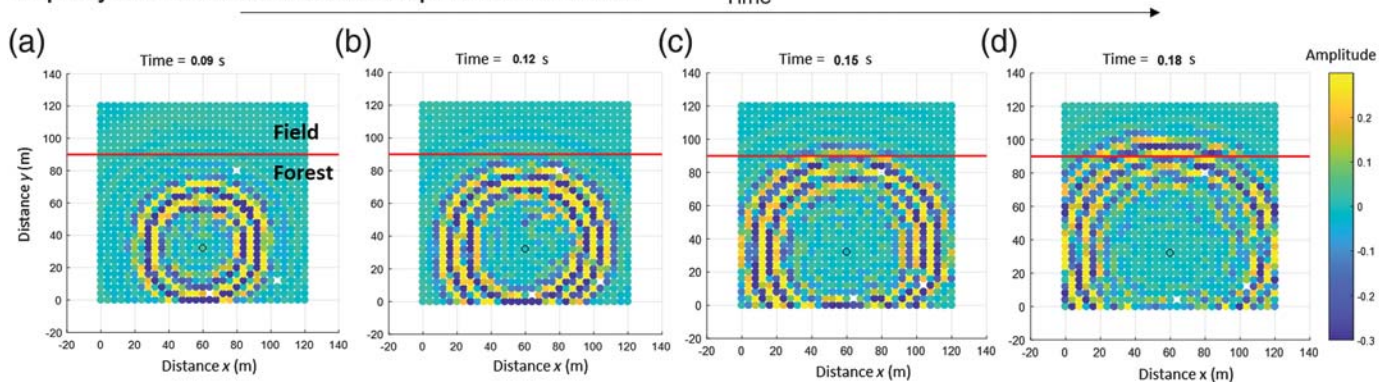
To confirm these observations, Figure 7 shows two series of four snapshots of the vertical wavefield measured in two frequency bands on the 2D grid of the Z-land sensors when the shaker emits from inside the forest. The wave patterns confirm the coherent wave propagation below the expected band gap F_c , and the strong damping and incoherent propagation observed above F_c . This result is consistent with the trees behaving as local resonators for surface wave propagation. However, a quantitative distinction between intrinsic attenuation of the subsurface soil above $F_c = 50 \text{ Hz}$ and scattering

attenuation due to the presence of trees will be the subject of further study.

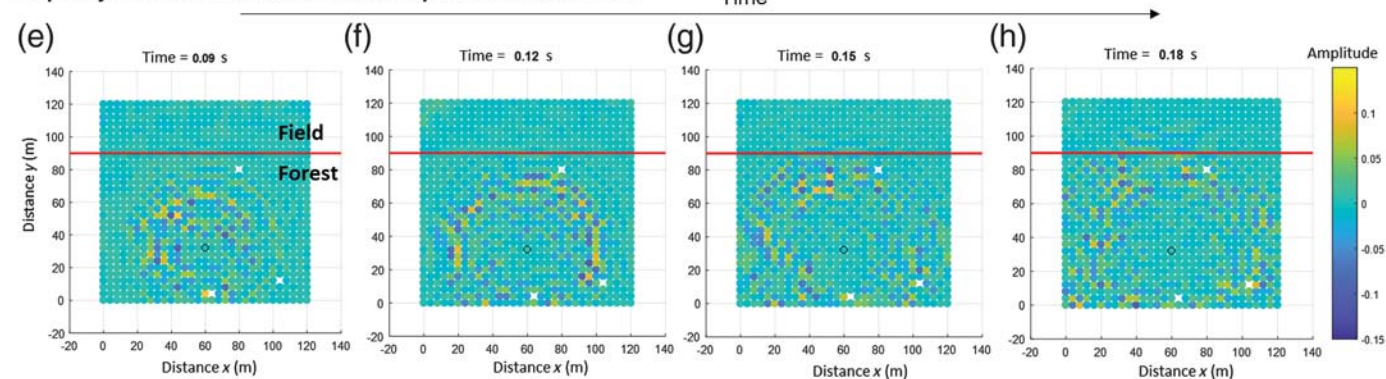
Below the 10-Hz minimum frequency of the shaker source, the cross-correlation wavefield captures the coherent part of the ambient noise field. At the zero time lag of the correlation, the focal spot emerges from the reconstructed converging/diverging wavefield as in a time-reversal experiment (Fink, 2006). The focal spots shown in Figure 8 are obtained from different 1-hr-long nighttime noise records at all of the stations that were cross correlated with data from one Z-land reference sensor positioned at the center of the sensor grid inside the forest. Figure 8a–c shows the focal spots obtained from narrowband correlations filtered around 4, 6, and 8 Hz. The time-reversal focal spot method is strongly connected to the spatial autocorrelation method (known as the SPAC method, see Aki, 1957; Hillers *et al.*, 2014). The overall symmetry of the focal spots confirms that the noise is omnidirectional inside the forest at low frequencies (Hillers *et al.*, 2016). From Figure 8, the first zero crossing of the focal spot amplitude gives a proxy for the seismic wavelength measurement, from which the surface-wave velocities can be extracted (Catheline *et al.*, 2008; Benech *et al.*, 2009; Gallot *et al.*, 2011).

The surface-wave dispersion curves were measured inside the forest for the frequency bands of both the shaker source ($> 15 \text{ Hz}$) and the ambient noise recordings ($< 15 \text{ Hz}$) from the data gathered from the GIPP 1D line array and the 2D Z-land array. Figure 9 shows the combination of active and passive data analysis for surface-wave phase velocities as a classical frequency–wavenumber representation. As expected at frequencies below F_c where the propagation behaves as in a spatially homogeneous effective medium, the dispersion curves depend neither on the source position nor on the particular day where the data have been recorded. A few particular points can be noted that confirm the locally resonant metamaterial behavior of the forest of trees. First, strong bending in the surface-wave

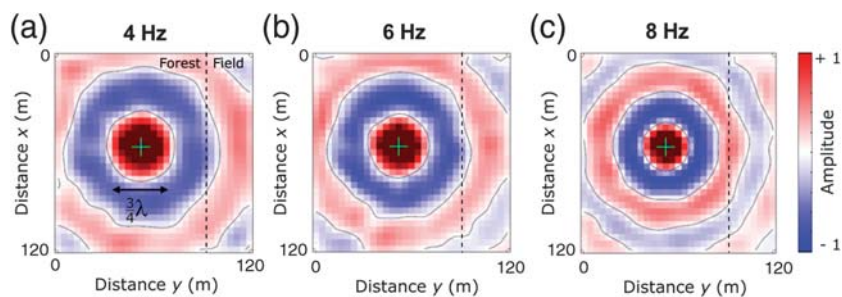
Frequency : 20 – 50 Hz : below the tree compressional resonances



Frequency : 50 – 80 Hz : above the tree compressional resonances

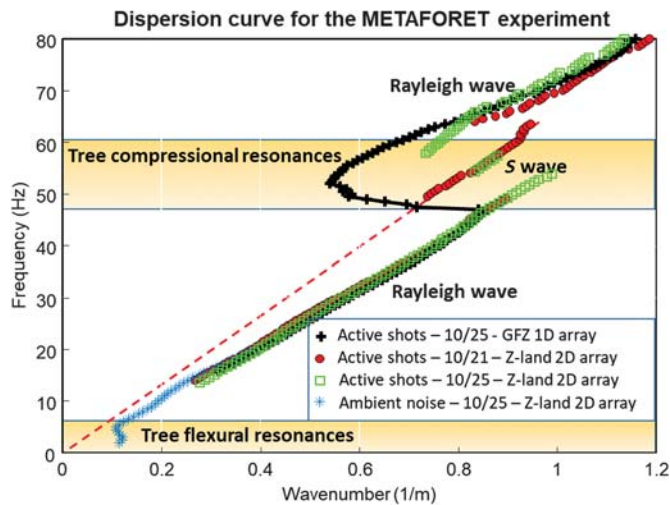


▲ **Figure 7.** (a–d) Spatial representation (x – y) of the seismic wavefield measured on the 2D Z-land seismic array for a source inside the forest at position ($x = 60$ m, $y = 30$ m) and displayed at four different snapshots: (from left to right) (a) $t = 0.09$ s, (b) $t = 0.12$ s, (c) $t = 0.15$ s, and (d) $t = 0.18$ s. The seismic wavefield has been filtered in the 20–50 Hz frequency band. In each panel, the horizontal red line represents the forest–field boundary. (e–h) Same representation as above for the seismic field filtered in the 50–80 Hz frequency band. The low-frequency part of the wavefield (< 50 Hz) shows a high-amplitude spatially coherent surface wave when the high-frequency part (> 50 Hz) has much weaker amplitude (see the different color bars in the top and bottom panels) and show incoherent spatial scattering.



▲ **Figure 8.** Zero lag amplitude distributions of narrowband filtered noise cross-correlation functions between the green-indicated reference sensor and all other sensors obtained from eight nighttime hours at three consecutive nights. The size of the focal spot indicated by the distance of the first zero crossing is equal to $3/4\lambda$ and behaves as a proxy for the local wavelength (λ) or phase speed. Warm (cool) colors represent positive (negative) amplitude values. Note that the images are rotated 90° clockwise with respect to the configuration in Figure 4. The dashed line shows the forest–field interface.

dispersion curve is observed between 45 and 60 Hz, in agreement with the tree compressional resonances (Fig. 5d). Because of the rapid velocity change, no energy propagation is possible in this frequency band, as confirmed by the surface-wave snapshots in Figure 7e–h. However, a direct S -body wave is still seen in this surface-wave band gap, as its polarization (mainly horizontal) might not couple well with the vertical trees inside the forest. Second, from the ambient noise recordings, another bending in the dispersion curve can be observed at low frequency (< 10 Hz). Indeed, as Rayleigh waves have an elliptical polarization, which implies both horizontal and vertical displacements, it is not surprising that the flexural resonance of the trees also couples with the seismic wavefield at low frequency. Where the surface-wave velocities should increase at low frequency, there was a maximum

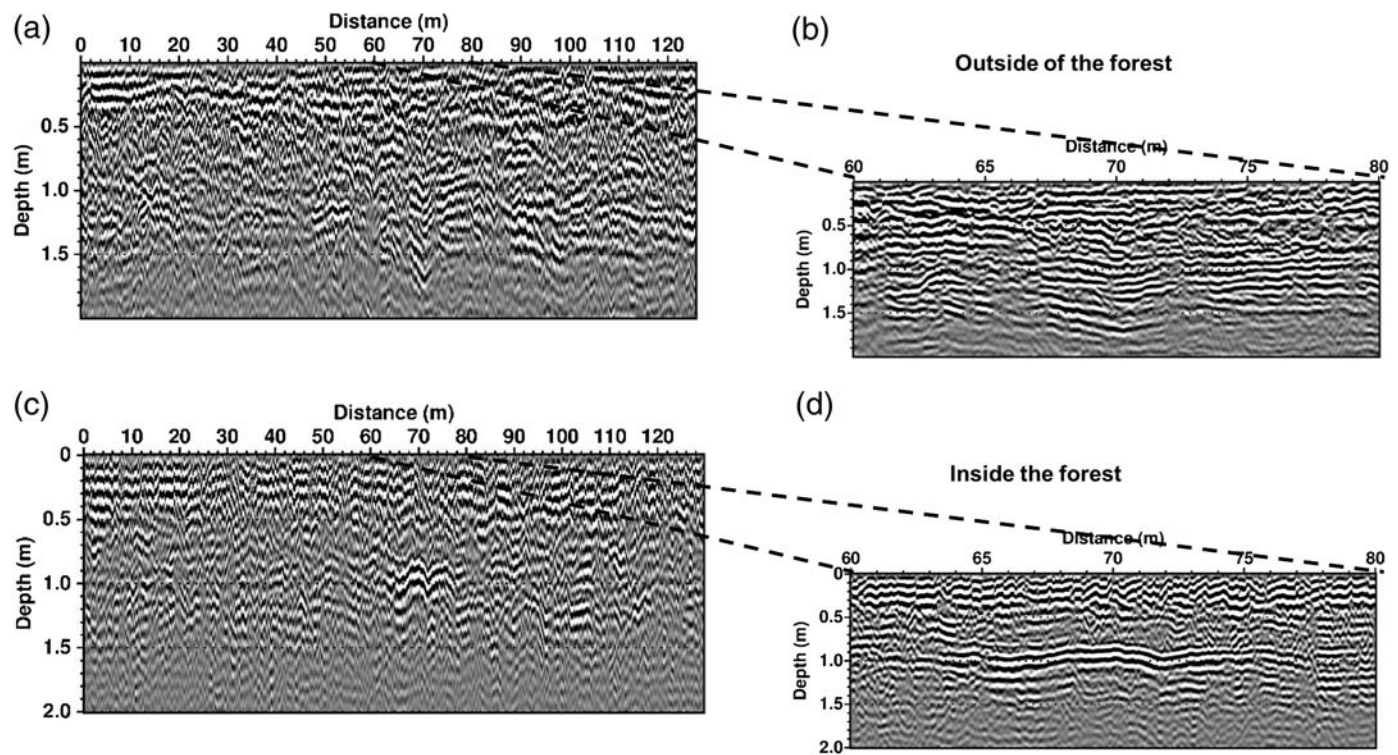


▲ **Figure 9.** Frequency–wavenumber representation of the surface-wave dispersion curves measured in the forest from ambient noise (blue) and active data (black, red, and green). Active data analysis (for different seismic acquisitions performed several days apart on 10/21 and 10/25) show high consistency both on the Z-land 2D array and the GIPP 1D array. Shaded colored areas refer to two frequency intervals associated with the tree compressional and flexural resonances. The main inflexion point in the dispersion curve between ~ 50 and ~ 60 Hz corresponds to a frequency band gap in agreement with the locally resonant metamaterial behavior of the forest.

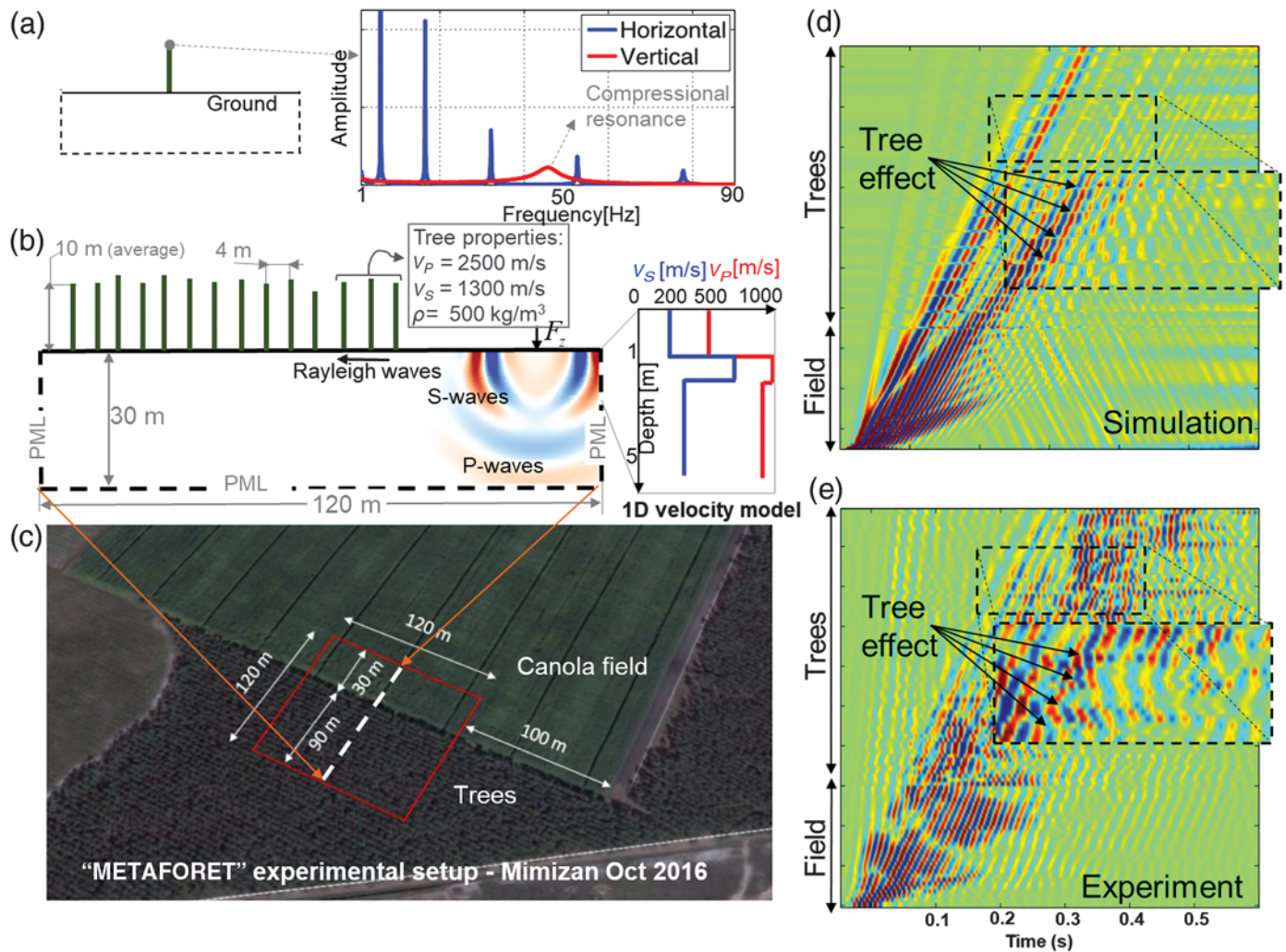
Rayleigh-wave phase velocity that was limited to 300 m/s at 2 Hz. This cannot be physically explained other than assuming the interference effect associated with trees behaving as coupled resonators at the subwavelength scale.

The Ground-Penetrating Radar Data

From all of the GPR profiles acquired, only two selected GPR images are shown in Figure 10, with two west–east lines shown after processing. The depth versus distance image (Fig. 10a) and a 20-m-long zoom (Fig. 10b) were acquired along line 26, which was located outside the forest, whereas the equivalent representation (Fig. 10c,d) corresponds to line 8 located within the forest. Each profile was processed using the Seismic Unix software (Stockwell, 1999) following a classical processing flow sequence for 2D GPR data (e.g., Cassidy, 2009). This includes a correction for time-zero drift, a 100–700-MHz band-pass filter to improve the signal-to-noise ratio, and an adapted “dewow” zero-phase low-cut filter that was designed to remove the continuous component or low-frequency bias in the data. In addition, ringing effects that manifest as nearly horizontal and periodic events were attenuated using a background removal technique. This attenuation includes direct airwave removal. The data were then migrated to relocate the actual reflections in their true 2D locations, then amplified as a function of time squared, and finally converted into depth. Common midpoint surveys acquired in various places with 200-MHz unshielded antennae allowed semblance analyses to be carried out. This



▲ **Figure 10.** Migrated GPR images obtained after classical processing of 500 MHz data. (a) Line 26 (outside of the forest) and (b) a 20-m-long zoom; (c) line 8 (within the forest) and (d) a 20-m-long zoom. Both images display numerous quasi-continuous reflectors within the first 2 m depth.



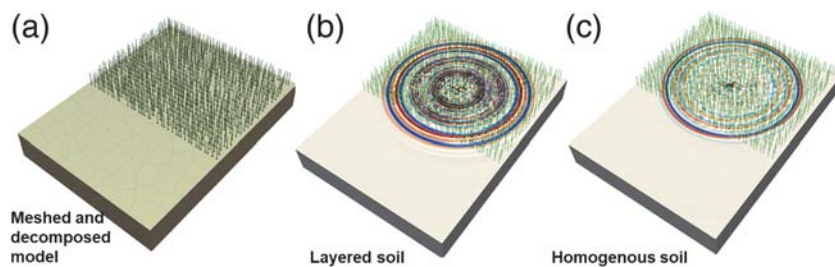
▲ **Figure 11.** Numerical simulations versus real data. (a) Frequency domain analysis of the motion of one tree (modeled as a uniform 2D beam) in the numerical simulations for a height of 9 m and a 0.4 m diameter. The blue curve depicts the horizontal motion characterized by flexural resonance peaks (above 1 Hz), while the red line depicts the vertical motion and the associated longitudinal motion resonance. Both measures are taken at the top of the tree. (b) Sketch of the 2D model used for the spectral element simulations with the average properties of the trees and one of the best-fitting velocity–depth profile extrapolated from the GPR sections. A snapshot of the wavefield shows how Rayleigh waves are generated from the vertical force at the surface. (c) Aerial view of the Mimizan experimental site showing the approximate location of the GIPP cube line used for the comparison. (d) Seismic section generated numerically using the model in (b) from a Ricker point source located outside the forest. The color code represents the vertical motion. (e) Same as (d) but for the experimental data from the GIPP cube line.

indicated a mean velocity of 7.6 cm/ns in the upper layers. This velocity was used for the migration algorithm and the time-to-depth conversion.

The 120-m-long GPR profiles show a large number of reflectors throughout the entire profile in the first 2 m depth, where the continuity is not obvious. The horizontal compression (120 m along the x axis, 2 m in depth) makes it difficult to visualize these reflectors. It is, however, noticeable that the profile located in the forest shows a large number of near-surface scattering points, which are certainly associated with trees and their roots. The migration algorithm was not able to resolve these scattering points in the imaging process. The 20-m-long

magnification is clearer. These show various reflectors with better continuity, one as particularly visible in the image of Figure 10d, at a depth of ~ 90 cm, which might be related to the top of a compacted sand interface. However, this does not appear to be continuous along the entire site. The decrease in the reflectivity at depths > 1.5 m might be related to the presence of the water table.

Using all of the GPR profiles, a careful pick of all of the reflectors should provide a pseudo-3D view of the heterogeneities in the whole site in the future, as performed by [Beauprêtre et al. \(2012\)](#) in their imaging of sedimentary interfaces shifted by successive earthquakes.



▲ **Figure 12.** (a) 3D model of the forest featuring accurate tree distribution and randomly distributed height. The 3D mesh is superimposed to the model showing the domain decomposition used in the parallel simulations. (b) Snapshot of the broadband field in a layered soil model (analogous to that in Fig. 11b). The color code represents the amplitude of the vertical component of the displacement with warm (cool) colors representing positive (negative) amplitude values. The source is located in the forest. (c) Same as (b) but for a homogenous velocity profile in the half-space with 400 and 1000 m/s for S - and P -wave velocities.

Numerical Simulations

The complex interactions between the surface waves and the trees can also be studied with the aid of numerical simulations, in particular when multiple factors might affect the wavefield such as soil layering and tree resonance. Here, we outline the methods and the preliminary results used to back the experimental observations. The backbone of this numerical section is the 2D and 3D numerical simulations, which were computed with the state-of-the-art, open-source, spectral-element-based code for elastodynamics problems known as SPEC-FEM2D/3D (Komatitsch and Tromp, 1999; Peter *et al.*, 2011). This code computes elastic wavefields with an incredible level of spatial and temporal detail and can tackle complex model geometries with subwavelength resonators. This time–spatial density thus allows detailed investigations into the interactions between the waves, the soil structure, and the trees. The 2D code solves the plain strain elastic problem (i.e., P – SV polarization), and given its reduced complexity, it is well suited for parametric analyses aimed at maximizing the fit to the data. As shown in Figure 11b, the soil is modeled using a half-space elastic domain with a free surface at the top (the top edge in 2D, the top surface in 3D) and perfectly matched layer conditions (Komatitsch and Martin, 2007) on the remaining lateral and bottom boundaries. The source is implemented as a vertical force, using a Ricker source time function centered at 50 Hz with the same bandwidth as the shaker source signal. The trees are modeled as longitudinally elongated beams (i.e., cantilever beams) attached without discontinuities to the surface of the half-space. The soil and trees are characterized by very different mechanical properties (e.g., Lamé parameters, density, and damping coefficient). The correct choice of these parameters is of crucial importance to understand the real observations. Numerical simulations were performed in a preliminary experiment (Colombi, Roux, *et al.*, 2016) to determine the best-fit mechanical parameters for wood. In the present study, the same parameters are used for the resonators (Fig. 11, see legend). As can be seen from Figure 11a,b, the numerical trees are characterized by both longitudinal and horizontal resonances, with a dynamic

response (neglecting the effects of damping) similar to those of the actual trees shown in Figure 5. Among the other parameters, the tree height drives the frequency of the compressional resonance. The large variation in the longitudinal and transverse dynamic responses is implemented in the simulations by randomizing the height and cross section of the trees. In the 2D case, the spacing between the trees is kept at 4 m, coherent with the tree layout in the y direction (Fig. 4). In the 3D simulations, the tree positions are accurately reproduced, as in Figure 4b.

Following the GPR data analysis, a layered soil model was implemented that approximates one of the active seismic sections along the GIPP line. Preliminary parametric analysis (mainly focused on thickness and shear-wave velocity of the soft layer) yields a numerical waveform that can qualitatively be compared with the actual one (Fig. 11d,e). Although the 1D model cannot completely explain all of the features observed in the real data, the effects of the trees are strikingly visible. A magnified image reveals the quasi-monochromatic oscillations that characterize the field in the forest in the proximity of the trees. These effects are also visible in Figure 11, and they appear to be stronger in the data than in the simulations. More work is needed to understand the coupling mechanism(s) and the energy transfer between the trees and the soil, as well as the role of intrinsic attenuation.

We now turn our attention to the 3D simulations. Figure 12a shows the complex 3D mesh model implemented for the simulations. Here, the focus is on the propagation from a source (Ricker time function, centered at 50 Hz) located inside the forest using a 1D stratified soil profile (Fig. 11b) and a homogenous one. In Figure 12b,c, two snapshots of the vertical component are shown that were taken a few milliseconds after the zero time of the source. In both cases, the scattering produced by the trees appears as a dominant feature. However, comparing Figure 12b,c, the resulting wavefields are also very sensitive to the soil layering. Compared to 2D code, the 3D simulations can combine the 2D attenuation of surface waves associated with scattering, absorption, and geometrical spreading in the x – y plane as well as the layered soil properties in the z direction. In particular, the 3D modeling clearly improves with the ability to separate the tree effects from the soil-layering effects. We expect them to provide a quantitative prediction of the effects of the trees in the real data (Fig. 6).

CONCLUSIONS

The METAFORÉ experiment was designed to demonstrate that complex wave physics phenomena classically observed at the mesoscales and microscales in acoustics and/or optics also apply at the seismic scale. In particular, the METAFORÉ experiment shows that a dense forest of trees can behave as a locally resonant metamaterial for seismic surface waves. It

creates frequency band gaps and anomalous dispersion curves. This experiment was made possible through the deployment of a seismic array of 1000 autonomous sensors that provided continuous recording of the vertical seismic wavefield at the transition between an open field and a dense forest. More equipments were deployed (e.g., GPR, velocimeters in trees, and shaker source), to allow for complementary geophysics measurements that validate the physical interpretations of the seismic wavefield observed.

DATA AND RESOURCES

Examples and guidelines for retrieval of the data and metadata can be downloaded from the ftp site: <ftp://metaforet@ist-ftp.ujf-grenoble.fr/>. The data access requires a password that can be obtained through an email sent to the corresponding author philippe.roux@univ-grenoble-alpes.fr. Because the raw data are too big (more than 2 TB in seed format) to be easily accessible and interpretable, we chose to isolate parts of the signals that correspond to:

1. passive data: a few hours of ambient noise signals on the 2D array of 961 vertical geophones and
2. active data: the seismic response to each of the 122 shaker sources excited in the zone of interest and measured both on the 2D array of vertical geophones and the 1D line of three-component 100 geophones.

The active data were cross correlated for pulse compression as described in this article and organized in different directories with MATLAB codes that provide representation tools of the seismic data. Word documents are added that describe the log of the experimental procedure for each source. Information on the tree positions and characteristics (heights and diameters) are also available. More information on the scientific objectives of the METAFORÉ project is available at <https://metaforet.osug.fr/>. The other data are from the following websites: fairfieldnodal.com/equipment/zland (FairField Nodal Inc.), www.gfz-potsdam.de/en/section/geophysical-deep-sounding/infrastructure/geophysical-instrument-pool-potsdam-gipp (GIPP), www.obspy.org (ObsPy functions), www.gfz-potsdam.de/en/section/geophysical-deep-sounding/infrastructure/geophysical-instrument-pool-potsdam-gipp/instruments/seismic-pool/recorder-dss-cube3/ (DATA-CUBE3), and www.gdsinstruments.com (GDS Inc.) All websites were last accessed in December 2017. ☒

ACKNOWLEDGMENTS

The authors wish to acknowledge Geokinetics USA Inc., Centre Régional de la Propriété Forestière Aquitaine, Mimizan City Hall, and Communauté de Commune for logistic efforts prior to and during the METAFORÉ experiment. The authors are personally grateful to Roland de Lary and Yvan Alquier for local help in Mimizan, and ISTerre students and Post-docs for practical help in the deployment and recovery of the Geophysical Instrument Pool Potsdam (GIPP) sensors and Z-land geophones. Cityshark and Lennartz velocimeters were provided by the Urban Seismology project at ISTerre, Greno-

ble. DATA-CUBE3 (with sensors) were provided by the GIPP at GFZ-Potsdam, under Grant Number 201626. The computations presented here were performed using the Froggy platform of the computing infrastructure CIMENT at Université Grenoble Alpes (UGA). The METAFORÉ project was funded by the French National Research Agency (ANR). This work was also supported by a grant from LabEx Osug@2020 under Contract Number ANR10LABX56. A. C. was supported by the Marie Curie Fellowship “Metacloak.” G. H. acknowledges support through a Heisenberg fellowship from the German Research Foundation (HI 1714/1-2).

REFERENCES

- Aki, K. (1957). Space and time spectra of stationary stochastic waves, with special reference to microtremors, *Bull. Earthq. Res. Inst.* **35**, 415–457.
- Beauprêtre, S., S. Garambois, I. Manighetti, J. Malavieille, R. Langridge, G. Sénéchal, M. Chatton, T. Davies, C. Larroque, D. Rousset, *et al.* (2012). Finding the buried record of past earthquakes with GPR-based paleoseismology: A case study on the Hope fault, New Zealand, *Geophys. J. Int.* **189**, no. 1, 73–100.
- Benech, N., S. Catheline, J. Brum, T. Gallot, and C. A. Negreira (2009). 1-D elasticity assessment in soft solids from shear wave correlation: The time-reversal approach, *IEEE Trans. Ultrason. Ferroelectrics Freq. Contr.* **56**, no. 11, 2400–2410.
- Beyreuther, M., R. Barsch, L. Krischer, T. Megies, Y. Behr, and J. Wassermann (2010). ObsPy: A Python toolbox for seismology, *Seismol. Res. Lett.* **81**, no. 3, 530–533.
- Brincker, R., L. Zhang, and P. Andersen (2001). Modal identification of output-only systems using frequency domain decomposition, *Smart Mater. Struct.* **10**, no. 3, 441.
- Brun, M., S. Guenneau, and A. B. Movchan (2009). Achieving control of in-plane elastic waves, *Appl. Phys. Lett.* **94**, no. 6, 061903.
- Cassidy, N. (2009). Ground penetrating radar data processing, modelling, and analysis, in *Ground Penetrating Radar: Theory and Applications*, H. M. Jol (Editor), Elsevier Science Ltd, Oxford, United Kingdom, 176 pp.
- Catheline, S., N. Benech, J. Brum, and C. Negreira (2008). Time reversal of elastic waves in soft solids, *Phys. Rev. Lett.* **100**, no. 6, 064301, doi: [10.1103/PhysRevLett.100.064301](https://doi.org/10.1103/PhysRevLett.100.064301).
- Chatelain, J. L., P. Guéguen, B. Guillier, J. Fréchet, F. Bondoux, J. Sarrault, P. Sulpice, and J. M. Neuville (2000). CityShark: A user-friendly instrument dedicated to ambient noise (microtremor) recording for site and building response studies, *Seismol. Res. Lett.* **71**, no. 6, 698–703.
- Clayton, R. W., and R. A. Wiggins (1976). Source shape estimation and deconvolution of teleseismic bodywaves, *Geophys. J. Int.* **47**, no. 1, 151–177.
- Colombi, A., S. Guenneau, P. Roux, and R. V. Craster (2016). Transformation seismology: Composite soil lenses for steering surface elastic Rayleigh waves, *Sci. Rep.* **6**, 25320.
- Colombi, A., P. Roux, S. Guenneau, P. Gueguen, and R. V. Craster (2016). Forests as a natural seismic metamaterial: Rayleigh wave bandgaps induced by local resonances, *Sci. Rep.* **6**, 19238.
- Engheta, N., and R. W. Ziolkowski (2006). *Metamaterials: Physics and Engineering Explorations*, John Wiley and Sons, New York, New York.
- Farhat, M., S. Guenneau, and S. Enoch (2009). Ultrabroadband elastic cloaking in thin plates, *Phys. Rev. Lett.* **103**, 024301.
- Fink, M. (2006). Time-reversal acoustics in complex environments, *Geophysics* **71**, no. 4, SI151–SI164, doi: [10.1190/1.2215356](https://doi.org/10.1190/1.2215356).
- Gallot, T., S. Catheline, P. Roux, and M. Campillo (2011). A passive inverse filter for Green’s function retrieval, *J. Acoust. Soc. Am.* **131**, no. 1, EL21–EL27.

- Guéguen, P., and P.-Y. Bard (2005). Soil-structure and soil-structure-soil interaction: experimental evidence at the Volvi test site, *J. Earthq. Eng.* **9**, no. 5, 657–693.
- Guéguen, P., and A. Colombi (2016). Experimental and numerical evidence of the clustering effect of structure on their response during earthquake: A case study of three identical towers in the city of Grenoble (France), *Bull. Seismol. Soc. Am.* **106**, no. 6, 2855–2864.
- Guéguen, P., P.-Y. Bard, and F. J. Chavez-Garcia (2002). Site-city interaction in Mexico City-like environments: An analytical study, *Bull. Seismol. Soc. Am.* **92**, no. 2, 794–811.
- Hillers, G., M. Campillo, Y. Ben-Zion, and P. Roux (2014). Seismic fault zone trapped noise, *J. Geophys. Res.* **119**, no. 7, 5786–5799.
- Hillers, G., P. Roux, M. Campillo, and Y. Ben-Zion (2016). Focal spot imaging based on zero lag cross-correlation amplitude fields: Application to dense array data at the San Jacinto fault zone, *J. Geophys. Res.* **121**, no. 11, doi: [10.1002/2016JB013014](https://doi.org/10.1002/2016JB013014).
- Kaina, N., M. Fink, and G. Lerosey (2013). Composite media mixing Bragg and local resonances for highly attenuating and broad bandgaps, *Sci. Rep.* **3**, 3240.
- Kittel, C., and P. McEuen (1976). *Introduction to Solid State Physics*, Vol. 8, Wiley, New York, New York.
- Komatitsch, D., and R. Martin (2007). An unsplit convolutional perfectly matched layer improved at grazing incidence for the seismic wave equation, *Geophysics* **72**, SM155–SM167.
- Komatitsch, D., and J. Tromp (1999). Introduction to the spectral element method for three-dimensional seismic wave propagation, *Geophys. J. Int.* **139**, no. 3, 806–822.
- Lemoult, F., M. Fink, and G. Lerosey (2011). Acoustic resonators for far-field control of sound on a subwavelength scale, *Phys. Rev. Lett.* **107**, 064301.
- Leonhardt, U. (2006). Optical conformal mapping, *Science* **312**, 1777.
- Liu, Z., X. Zhang, Y. Mao, Y. Y. Zhu, Z. Yang, C. T. Chan, and P. Sheng (2000). Locally resonant sonic materials, *Science* **289**, 1734.
- Michel, C., P. Guéguen, S. El Arem, J. Mazars, and P. Kotronis (2010). Full scale dynamic response of a RC building under weak seismic motions using earthquake recordings, ambient vibrations and modeling, *Earthq. Eng. Struct. Dynam.* **39**, 419–441.
- Milton, G., M. Briane, and J. Willis (2006). On cloaking for elasticity and physical equations with a transformation invariant form, *New J. Phys.* **8**, no. 248, 014301.
- Nakata, N., and R. Snieder (2014). Monitoring a building using deconvolution interferometry. II: Ambient-vibration analysis, *Bull. Seismol. Soc. Am.* **104**, no. 1, 204–213.
- Pendry, J. B. (2000). Negative refraction makes a perfect lens, *Phys. Rev. Lett.* **85**, 3966–3969.
- Pendry, J. B., A. J. Holden, D. J. Robbins, and W. J. Stewart (1999). Magnetism from conductors and enhanced nonlinear phenomena, *IEEE Trans. Microwave Theory Tech.* **47**, 2075.
- Pendry, J. B., D. Schurig, and D. R. Smith (2006). Controlling electromagnetic fields, *Science* **312**, 1780.
- Peter, D., D. Komatitsch, Y. Luo, R. Martin, N. Le Goff, E. Casarotti, P. Le Loher, F. Magnoni, Q. Liu, C. Blitz, *et al.* (2011). Forward and adjoint simulations of seismic wave propagation on fully unstructured hexahedral meshes, *Geophys. J. Int.* **186**, no. 2, 721–739.
- Rupin, M., S. Catheline, and P. Roux (2015). Super-resolution experiments on Lamb waves using a single emitter, *Appl. Phys. Lett.* **106**, 24103.
- Rupin, M., F. Lemoult, G. Lerosey, and P. Roux (2014). Experimental demonstration of ordered and disordered multiresonant metamaterials for Lamb waves, *Phys. Rev. Lett.* **112**, 234301.
- Stockwell, J. W., Jr. (1999). The CWP/SU: Seismic Un*x Package, *Comput. Geosci.* **25**, no. 4, 415–419.
- Zhu, J., J. Christensen, J. Jung, L. Martin-Moreno, X. Yin, L. Fok, X. Zhang, and F. J. Garcia-Vidal (2011). A holey-structured metamaterial for acoustic deep-subwavelength imaging, *Nature Phys.* **7**, 52.

Philippe Roux
 Isabelle Douste-Bacque
 Stéphane Garambois
 Philippe Gueguen
 Gregor Hillers¹
 Ildut Pondaven
 ISTERre, CNRS UMR 5275, IFSTTAR
 Université Grenoble Alpes
 Campus Universitaire
 1381, rue de la Piscine
 38041 Grenoble Cedex 9
 France
philippe.roux@univ-grenoble-alpes.fr

Dino Bindi
 Tobias Boxberger
 Fabrice Cotton
 Helmholtz Centre Potsdam
 GFZ German Research Centre for Geosciences
 Public Law Foundation State of Brandenburg
 Telegrafenberg, D-14473 Potsdam
 Germany

Andrea Colombi
 Department of Mathematics
 Imperial College London
 South Kensington Campus
 London SW7 2AZ, United Kingdom

Dan Hollis
 Sisprobe Inc.
 24 Allée des Vulpains
 38240 Meylan
 France

Thomas Lecocq
 Royal Observatory of Belgium
 Ringlaan 3
 1180 Brussels, Belgium

Published Online 10 January 2018

¹ Now at Institute of Seismology, University of Helsinki, Helsinki, Finland.